ADVANCED MATERIALS
www.advmat.de

Polarization- and Gate-Tunable Optoelectronic Reverse in 2D Semimetal/Semiconductor Photovoltaic Heterostructure

Hanyu Wang, Yan Li, Peng Gao, Jina Wang, Xuefeng Meng, Yin Hu, Juehan Yang, Zihao Huang, Wei Gao, Zhaoqiang Zheng, Zhongming Wei, Jingbo Li,* and Nengjie Huo**

Polarimetric photodetector can acquire higher resolution and more surface information of imaging targets in complex environments due to the identification of light polarization. To date, the existing technologies yet sustain the poor polarization sensitivity (<10), far from market application requirement. Here, the photovoltaic detectors with polarization- and gate-tunable optoelectronic reverse phenomenon are developed based on semimetal 1T′-$MoTe_2$ and ambipolar WSe_2. The device exhibits gate-tunable reverse in rectifying and photovoltaic characters due to the directional inversion of energy band, yielding a wide range of current rectification ratio from 10^{-2} to 10^3 and a clear object imaging with 100 × 100 pixels. Acting as a polarimetric photodetector, the polarization ratio (PR) value can reach a steady state value of ≈30, which is compelling among the state-of-the-art 2D-based polarized detectors. The sign reversal of polarization-sensitive photocurrent by varying the light polarization angles is also observed, that can enable the PR value with a potential to cover possible numbers (1→+∞/-∞→−1). This work develops a photovoltaic detector with polarization- and gate-tunable optoelectronic reverse phenomenon, making a significant progress in polarimetric imaging and multifunction integration applications.

1. Introduction

The development of polarimetric photodetection technology is of great significance for the military and civilian fields such as biological imaging, optical radar, night vision, and remote sensing.[1–3] That benefits from the sensitive detection of light polarization alongside the intensity and wavelength, enabling the imaging with higher resolution and more surface information in darkness and foggy environment.[3] The early polarization-sensitive photodetectors are often equipped with additional components such as polarizers, gratings and polarization dielectric films,[4] that increases the size, cost and fabrication complexity of the device, impeding commercialization in high volume consumer electronics.

In recent years, anisotropic low-dimensional materials have been exploited as a new class of active film for polarization-sensitive photodetector.[5–8] For example, 1D GaN and ZnO nanowires have been demonstrated to have the capability to distinguish the light polarization in ultraviolet spectral region due to their anisotropic geometric effect, but suffer from the harsh targeting and calibration procedures as well as poor polarization sensitivity. As a more appealing candidate, 2D materials with in-plane anisotropic crystal structure attract numerous attentions for polarization-sensitive application due to their exotic physical properties and atomically smooth surface

H. Wang, P. Gao, J. Wang, X. Meng, W. Gao, N. Huo
School of Semiconductor Science and Technology
South China Normal University
Foshan 528225, P. R. China
E-mail: njhuo@m.scnu.edu.cn
Y. Li
State Key Laboratory for Mechanical Behavior of Materials
Xi′an Jiaotong University
Xi'an 710049, P. R. China
Y. Hu, J. Yang, Z. Wei
State Key Laboratory of Superlattices and Microstructures
Institute of Semiconductors
Chinese Academy of Sciences
Beijing 100083, P. R. China
E-mail: zmwei@semi.ac.cn
Z. Huang, Z. Zheng
Guangdong Provincial Key Laboratory of Information Photonics Technology
School of Materials and Energy
Guangdong University of Technology
Guangzhou 510006, P. R. China
J. Li
College of Optical Science and Engineering
Zhejiang University
Hangzhou 310027, P. R. China
E-mail: jbli@zju.edu.cn
N. Huo
Guangdong Provincial Key Laboratory of Chip and Integration Technology
Guangzhou 510631, P. R. China

The ORCID identification number(s) for the author(s) of this article can be found under https://doi.org/10.1002/adma.202309371

DOI: 10.1002/adma.202309371

without dangling bonds, that promises the seamless integration with current mature complementary metal-oxide-semiconductor (CMOS) process lines.[9–11] Among them, black phosphorous (BP), ReS_2, GeSe, etc., have been widely explored as promising 2D anisotropic semiconductors in the polarimetric photodetectors.[12–14] Meanwhile, the 2D semimetals such as 1T′-$MoTe_2$, 1T′-WTe_2 and $TaIrTe_4$ also stand out because of the topological band structure and potentials in near- and mid-wave infrared polarization-sensitive photodetector.[15–17] Recently, the mid- and long-wave infrared (IR) polarization-sensitive photodetectors comprising a perfect plasmonic absorber or chiral plasmonic metamaterial relying on photothermoelectric (PTE) effect,[18–20] as well as the twisted unipolar-barrier b-AsP based heterostructure[21] have also been demonstrated to exhibit high polarization sensitivity and application potential in miniaturized IR polarimeters.

Though some progress has been made, the existing technologies have still lagged behind expectations particularly in the aspect of the low polarization ratio (PR) value less than 10. The previous polarimetric photodetectors mainly recognize the polarization of incident light through the magnitude change of photocurrent due to the anisotropic absorption, the inherent operation mechanism eventually limits the polarimetric sensitivity and identification accuracy. On the other hand, the sign reversal of photocurrent by varying the light polarization could offer a unique opportunity for next-generation polarimetric imaging with higher resolution. To achieve the polarization-sensitive photocurrent flipping, noncentrosymmetric metallic nanoantennas have been integrated with semimetal or ferroelectrics based detectors,[22–24] which however suffer from the rigorous design of antenna orientation and complex fabrication process.

At the same time, the optoelectronic reverse such as bidirectional rectifying and photocurrent flipping induced by light polarization are particularly important factors to integrate the multiple functional modules into a single module, realizing "All-in-one" system, such as sensing and computing integrated technology, artificial neural network technology, vision acquisition and processing integrated technology. However, the reverse phenomenon by gate-voltage and polarization in 2D device still remains rarely studied.

In this work, the van der Waals (vdW) photovoltaic detectors based on semimetal 1T′-$MoTe_2$ and semiconductor WSe_2 are fabricated to realize the optoelectronic reverse with bidirectional rectifying and photoresponse behavior. The Fermi level in ambipolar WSe_2 can be tuned between conduction band (CB) and valence band (VB) by the gate voltage, leading to a large modulation of energy band at vdW Schottky junctions. As a result, the built-in electric field is readily regulated and inverted. Thus, the device exhibits a reversible rectifying behavior with a wide range of current rectification ratio from 10^{-2} to 10^3 due to a directional inversion of Schottky junction. Under light illumination, the device also has well gate-tunable and reversible photovoltaic properties, enabling the clear object imaging with responsivity of 212.15 mA W^{-1}, dynamic response of ≈0.1 ms and photo−dark current ratio (*PDCR*) over 10^5 (153.99 mW cm^{-2}). Leveraging the in-plane anisotropic structure of 1T′-$MoTe_2$, the device achieves a highly efficient capability of polarimetric detection with PR value up to ≈30, yielding a high anisotropy in responsivity, detectivity and *PDCR*, which endows the device with widespread application potential in ultra-compact polarimeters. More interestingly, the polarization sensitivity varies with gate voltage and undergoes a sign reversal, namely, the polarized light excited photocurrent is also reversed between negative and positive states by changing the polarization angles. The ability of photocurrent flipping induced by light polarization is of great interest to recognize the polarization signal more accurately.

2. Results and Discussion

2.1. Characterization of vdW Schottky Heterojunctions

The van der Waals (vdW) photovoltaic heterostructure was designed by stacking multilayer semimetal 1T′-$MoTe_2$ on top of semiconducting WSe_2 on 300 nm SiO_2/Si substrate, using the PVA (polyvinyl alcohol)/PDMS (polydimethylsiloxane) assisted dry transfer technique (see details in device fabrication section). The Au electrodes were deposited via ultraviolet lithography and electron-beam evaporation techniques. **Figure 1a** illustrates the crystal structures and the schematic diagram of the 1T′-$MoTe_2$/WSe_2 heterostructure, in which, a vertical built-in electric field can form at the junction interface and facilitate the separation of photoexcited electron-hole pairs. Figure 1b shows the schematic and optical microscopy image of the device where the source, drain and gate terminals are located at WSe_2, 1T′-$MoTe_2$ and bottom Si, respectively. The Raman scattering and PL spectrum were measured, as shown in Figure 1c,d. respectively. The Raman peaks at 247 and 253 cm^{-1} are corresponding to $E^1{}_g$ (in-plane) and $A^1{}_g$ (out-of-plane) modes of WSe_2, while the A_g (74.86, 125.21, 159.73, 257.34 cm^{-1}) and B_g (107.88 cm^{-1}) modes are typical Raman modes of 1T′-$MoTe_2$. All the phonon modes are observed in the heterojunction area. From Figure 1d, the multilayer WSe_2 has PL peaks at 780 and 905 nm, which are attributed to its direct bandgap of 1.58 eV and indirect bandgap of 1.39 eV, while 1T′-$MoTe_2$ has no luminescence because of its semimetal feature. Due to the strong interlayer coupling, the PL of WSe_2 is much reduced in junction, indicating the efficient separation of photocarrier. The PL quenching is also observed in the heterostructure with WSe_2 placed on top of 1T′-$MoTe_2$ layer as shown in Figure S1 (Supporting Information), that can exclude the shielding effect of 1T′-$MoTe_2$.

Figure 1e shows the cross-sectional high-resolution transmission electron microscopy (HRTEM) images of the Schottky junction (1T′-$MoTe_2$/WSe_2), where all the stacked van der Waals (vdW) layers exhibit clear lattice fringe and atomically-smooth interfaces, implying high quality of 2D crystal and vdW interface. The interplanar spacings of 1T′-$MoTe_2$ and WSe_2 are measured to be 0.70 nm and 0.65 nm. The corresponding element mapping by energy dispersive spectroscopy (EDS) further confirms the components of the heterostructure, as shown in Figure 1f and Figure S2 (Supporting Information). To further characterize the Schottky junction, the surface potential difference (SPD) of 1T′-$MoTe_2$/WSe_2 interface (Figure S3, Supporting Information) was obtained by the Kelvin probe force microscopy (KPFM) instrument. And the ΔE_F can be calculated to be ≈20 meV, which can lead to the formation of built-in electric field when it reaches equilibrium state after contact.

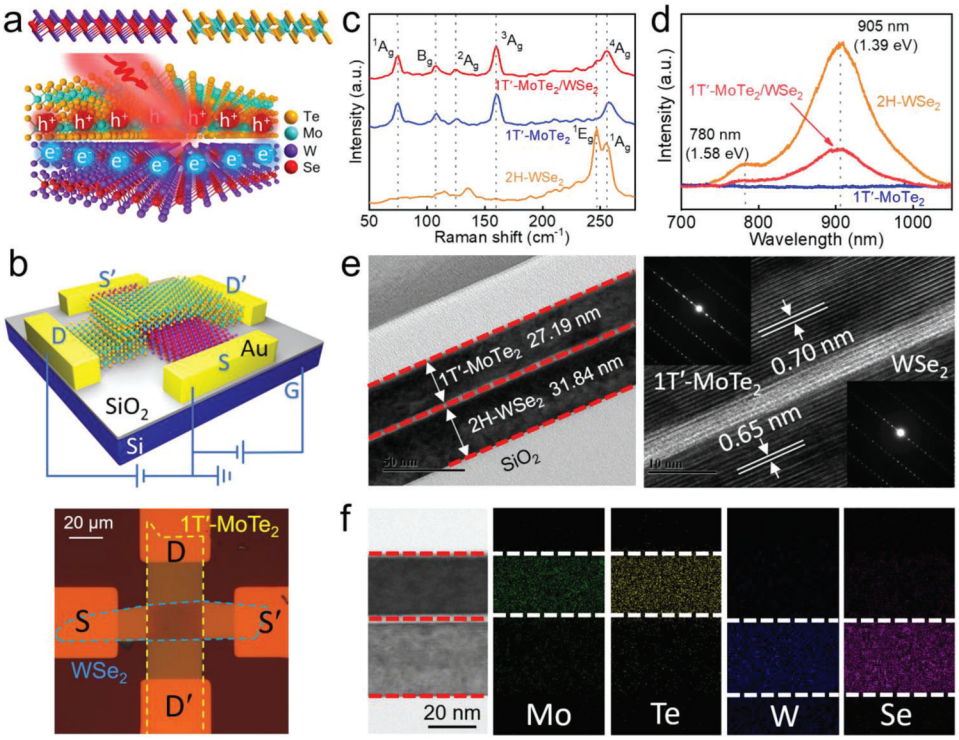

Figure 1. Characterizations of 1T′-$MoTe_2$/WSe_2 Schottky junction. a) Atomic structure and schematic diagram of photocurrent generation. b) Schematic diagram (top panel) and optical microscopy image (bottom panel) of the photovoltaic detector. Raman scattering c) and photoluminescence d) spectrum of 1T′-$MoTe_2$, WSe_2 and Schottky junction. e) Cross-sectional transmission electron microscopy image and SAED pattern of 1T′-$MoTe_2$/WSe_2. Scale bar: 50 nm (10 nm). f) Element mapping of the Schottky junction (heavy atoms: tellurium (Te), Molybdenum (Mo), tungsten (W) and selenium (Se)). Scale bar: 20 nm.

2.2. Reverse in Rectifying and Energy Band

As control devices, the electrical properties of individual 1T′-$MoTe_2$ and WSe_2 were measured, as shown in Figure S4a,b (Supporting Information). From *I–V* and transfer curves, no current rectification behavior is observed for both devices. The 1T′-$MoTe_2$ shows the metallic electrical feature with current on the level of milliampere, while the WSe_2 exhibits a semiconducting and ambipolar behavior. To be in contrast, the 1T′-$MoTe_2$/WSe_2 heterojunction exhibits obvious rectifying characteristic in Figure S4c, implying the existence of Schottky barrier at junctions. It is interesting that the current rectification can be modulated and inverted by the gate voltage, yielding the electrical reverse with bidirectional rectifying behavior. When the gate voltage is swept from −5 V to −40 V (**Figure 2a**), the reverse current increases gradually, while the forward current is suppressed. On the contrary, the forward current increases and the reverse state remains off when sweeping the gate voltage from 0 to 40 V (Figure 2b). Thus, our Schottky device exhibits the great gate-modulation of current rectification in terms of its ratio and direction, which is distinct from the electrical characteristic of a classical diode. The extracted *I–V* curves at negative (−25 V), zero (0 V) and positive (25 V) gate voltage (Figure S5a, Supporting Information) clearly demonstrate the reconfigurable and bidirectional rectifying behavior by applying V_G from negative to positive.

Further, the current rectification ratio (R_{rec}) is defined as a value by dividing the current at V_{DS} of 1 V over that at V_{DS} of −1 V ($R_{rec} = I_{V_{DS}=1\ V} / I_{V_{DS}=-1\ V}$). Figure 2c plots the rectification ratio as a function of gate voltage, two regions are basically divided, where the region I is the reverse on-state with ratio of 2.7×10^{-2}, and region II represents the forward on-state with ratio up to 5.7×10^{3}. This suggests a wide range of modulation on rectification ratio exceeding 10^5 by the gate voltage, providing a potential prospect in rectifier and inverter application.

To figure out the underlying mechanism, the energy band structures of 1T′-$MoTe_2$ and WSe_2 were calculated through first-principles calculations. Figure 2d shows the band structure of 1T′-$MoTe_2$, the valence band (blue line) is partially overlapping with the conduction band (red line), implying the semimetal feature. For multilayer WSe_2 (Figure 2e), the conduction band minimum (CBM) is located at a point along the K–Γ line, and the valance band maximum (VBM) is located at Γ point, showing an indirect bandgap. The work function, i.e., position of Fermi level of WSe_2 with respect to the vacuum level, has also been calculated as function of charge doping concentration (Figure 2f), the back-gate induced electron (hole) doping can decrease (increase) the work function of WSe_2. The Fermi level of pristine 1T′-$MoTe_2$ is fixed at about −4.45 eV.

Based on the above calculation results, the schematic diagram of energy band of the 1T′-$MoTe_2$/WSe_2 junction at different conditions are plotted, as shown in Figure 2g–i. Before contact, the positions of energy band are determined from theoretical results, showing a large band offset between 1T′-$MoTe_2$ and WSe_2

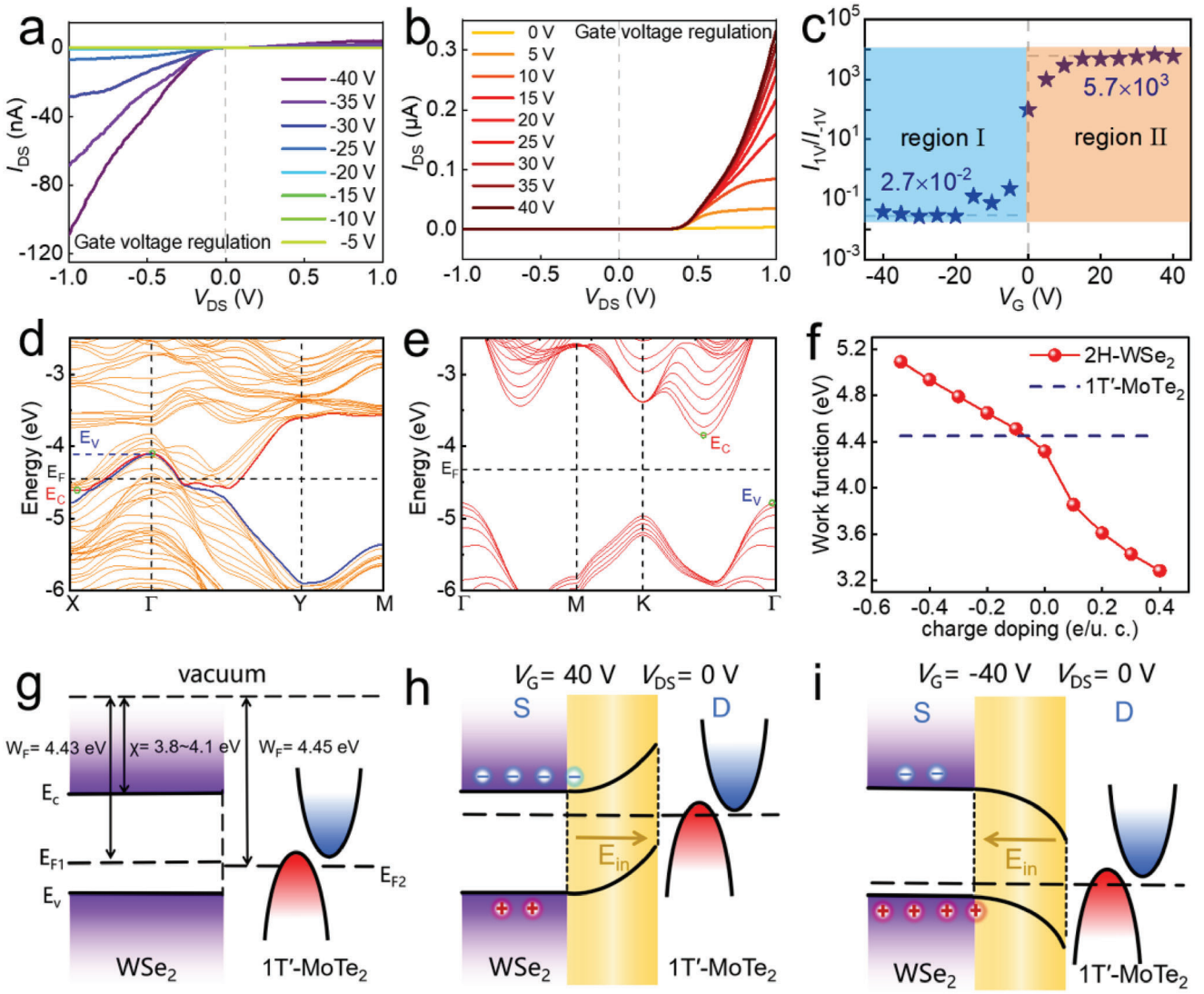

Figure 2. Gate-tunable and reversible rectifying and energy band modulation in the device. a,b) Output curve of the device at negative V_G (−40 to −5 V) and positive V_G (0–40 V), respectively, showing the bidirectional rectifying behavior. c) Current rectification ratio as a function of V_G at $V_{DS} = \pm 1$ V. d,e) Calculated energy band structure of multilayer 1T′-$MoTe_2$ and WSe_2, respectively. The vacuum level is set to 0 eV. f) Work function of WSe_2 as function of charge doping concentration. The blue dashed line denotes the work function of pristine 1T′-$MoTe_2$. Energy band diagram of the Schottky junction before contact g), at V_G of 40 V h) and at V_G of −40 V i), showing the gate-tunable band bending and built-in field.

(Figure 2g), the Fermi level difference (ΔE_F) is ≈20 meV from the KPFM result which can lead to a slight band bending and built-in electric filed (E_{in}) with direction from WSe_2 to 1T′-$MoTe_2$ (Figure S5b in the Supporting Information). As shown in Figure 2f, the charge doping can significantly modulate the work function of WSe_2, while has no influence on that of 1T′-$MoTe_2$. By applying the positive V_G (40 V), the Fermi energy level of WSe_2 is shifted upward close to its conduction band due to the electron doping, this can enlarge ΔE_F and strengthen E_{in} with wider depletion region and sharper upward bending of energy band in Figure 2h. In such case, the Schottky junction is turned on (off) when a forward (reverse) bias is applied, leading to a forward current rectification up to 5.7×10^3. On the other hand, the Fermi level of WSe_2 moves to its valence band because of the hole doping by applying the negative V_G (−40 V), the energy band of WSe_2 starts to bend downward and the direction of E_{in} is inverted from 1T′-$MoTe_2$ to WSe_2 as shown in Figure 2i. Thus, the Schottky junction is turned on (off) when a reverse (forward) bias is applied, resulting in a reverse current rectification as low as 10^{-2}. Furthermore, the measured gate-dependent KPFM also confirms the energy band modulation and the reverse of E_{in} direction, which is in accordance with theoretical calculation results (see details in Figure S6 in the Supporting Information). Leveraging the ambipolar character of WSe_2, the built-in electric field (E_{in}) and energy band arrangement of the Schottky junction is regulated and inverted by varying the back gate voltage, leading to an interesting gate-tunable and reversible rectifying behavior with a wide range of current rectification ratio exceeding 10^5.

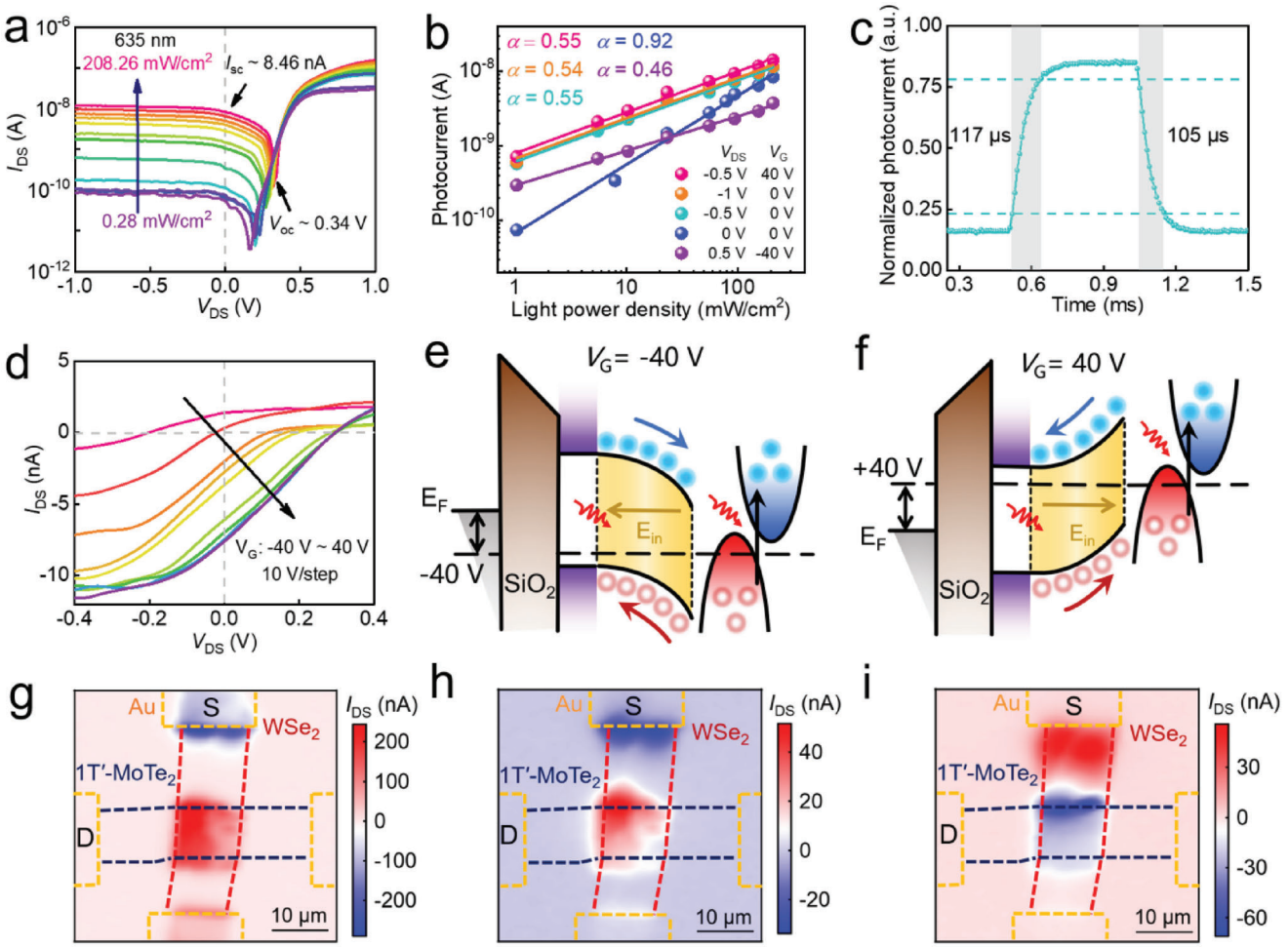

Figure 3. Reversible photovoltaic and photoresponse properties. a) I_{DS}–V_{DS} curves under 635 nm illumination with different light power density. b) Extracted photocurrent as function of light power density at 635 nm for different gate and bias voltages. c) Temporal response at V_{DS} = 0 V for estimating the raise and decay time. d) I_{DS}–V_{DS} curves by sweeping V_G from −40 to 40 V under light illumination with a power density of 55.71 mW cm^{-2}. e,f) Schematic diagram of energy band and photocarrier drift in the device at V_G of −40 and V_G of 40 V, respectively. The blue and red balls (arrow) represent the photogenerated electrons and holes (transport direction), respectively. g–i) Scanning photocurrent mapping of the device under 638 nm light illumination at 0 V bias voltage and different gate voltages (−40, 0, and 40 V, respectively).

2.3. Reversible and High Efficient Photovoltaic Properties

The photodetector at zero bias and gate voltage is further quantitatively characterized. **Figure** 3a and Figure S7 (Supporting Information) show the I_{DS}–V_{DS} curves at different gate voltages (V_G = 0, −40, and 40 V, respectively) under 635 nm light illumination with varying light power intensity, demonstrating a significant photovoltaic effect. The photocurrent (I_{ph}) as function of light power density at different bias (V_{DS} and V_G) conditions has been extracted in Figure 3b. The relationship between I_{ph} and light power density can be well fitted using power-law formula: $I_{ph} \propto P^{\alpha}$, where I_{ph}, P and α represent the photocurrent, light power density and fitting index, respectively. It is observed that the bias conditions have significant influence on the relationship between photocurrent and light power density. For V_G = 0 V, the fitting index (α) values of the device at V_{DS} = 0, −0.5, and −1 V are fitted to be 0.92, 0.55, and 0.54, respectively. At $|V_{DS}|$= 0.5 V, the α values are 0.46, 0.55 and 0.55 for V_G of −40, 0, and 40 V, respectively. The output electrical power (defined as $P_{el} = V_{DS} \times I_{DS}$), fill factor (FF) and power conversion efficiency (defined as $PCE = max\ (P_{el})\ /\ P_{in}$) as a function of light power density are also evaluated (Figure S8a–c in the Supporting Information). The maximum FF and PCE at 635 nm can reach up to 64% and 2.12%, respectively, implying a well-designed photovoltaic device considering its atomically thin profile.

The photovoltaic performances in terms of the key figure-of-merit are also measured and assessed, which include noise spectral density (S_n), responsivity (R), specific detectivity (D^*), and photo−dark current ratio ($PDCR$). The detailed data and analysis can be found in Supporting Information (Figures S8 and S9, Supporting Information). Briefly, the S_n as a function of frequency (f) contains two common regions: $1/f$ noise and white noise as low as ≈5 fA Hz$^{-1/2}$. At 635 nm laser illumination, the device exhibits remarkable photodetection performances with R of 212.15 mA W^{-1}, D^* of ≈4 × 10^{10} Jones, $PDCR$ of 10^5 (153.99 mW cm^{-2}),

which are very competing compared to those in the currently developed 2D-based photovoltaic detectors.[25–27] It is noted that the device also possesses the ability to detect the light in the near- and mid-wavelength infrared range (1.55 and 4.05 μm) measured by a high precision photocurrent scanning test microscope system as shown in Figures S10,S11 (Supporting Information), which can be attributed to the zero band gap of 1T′-$MoTe_2$ component, implying a great application potential in infrared photodetectors.

In order to enable a wide range of applications for image sensing, the detector usually requires a fast response speed and high stability. As shown in Figure 3c, our device exhibits a fast temporal response with raise time (τ_{raise}) of 117 μs and decay time (τ_{dec}) of 105 μs. To verify imaging quality, the detectors are integrated with an imaging measurement system (Figure S8g, Supporting Information) to achieve a high-resolution mapping image with 100 × 100 pixels and clear boundaries (Figure S8h, Supporting Information), that shows the great application potential of the vdW Schottky junction in image sensors. The photoswitching behavior has no degradation after hundreds of cycles, revealing well repeatability and stability of our device (Figure S12, Supporting Information).

As a vdW Schottky diode, our device exhibits not only a wide range gate-tunable rectification characteristic but also a reversible photovoltaic performance. Figure 3d shows the I_{DS}–V_{DS} curves at different V_G under 635 nm light illumination with power density of 55.71 mW cm^{-2}. It is observed that the photovoltaic effect can also be gradually modulated by the gate voltage, both open circuit voltage (V_{OC}) and short circuit current (I_{SC}) have a sign reversal by applying V_G from -40 to 40 V, this reversible photovoltaic phenomenon is in accordance with energy band evolution as discussed above. Under light illumination, the photoexcited electrons and holes can be separated by the built-in electric field at junction and collected by the electrodes to form the photocurrent (i.e., I_{SC}). As shown in Figure 3f, the energy band bends upward and the direction of E_{in} is from WSe_2 to 1T′-$MoTe_2$ at V_G of 40 V, thus the photogenerated electrons and holes move to WSe_2 and 1T′-$MoTe_2$, respectively, leading to negative I_{SC} and positive V_{OC}. At V_G of −40 V, the energy band bends downward with inverted E_{in} as shown in Figure 3e, causing an opposite I_{SC} and V_{OC} as well.

To further investigate the origin of photocurrent, the scanning photocurrent mapping of the Schottky photovoltaic device at zero bias and different V_G are measured. As shown in Figure 3g–i, the photocurrent mapping of the device at V_G = -40, 0, and 40 V are illustrated, respectively. It can be observed that the photocurrent of the device mainly originates from two regions, one is the photocurrent formed in the contact region between WSe_2 and Au electrode, and the other is from the vdW Schottky junction region between WSe_2 and 1T′-$MoTe_2$. At V_G = 0 V (Figure 3h), both distribution area and absolute value of the photocurrent at WSe_2/1T′-$MoTe_2$ junction are larger than that at Au/WSe_2 region, indicating that the dominated photocurrent is from the WSe_2/1T′-$MoTe_2$ junction. At V_G of −40 V (Figure 3g) and 40 V (Figure 3i), the photocurrent distributed in both regions undergoes a simultaneous reverse by changing the gate voltage from negative to positive, confirming the existence of the reversible photovoltaic effect.

2.4. Polarimetric Photodetection with High Polarization Ratio

As a key figure of merit, the capability of polarization-sensitive photodetection of our detector is also assessed. The angle-resolved polarized Raman spectroscopy (ARPR) of semimetal 1T′-$MoTe_2$ has been measured to demonstrate its strong in-plane anisotropic crystal structure (see details in Figure S13, Supporting Information), which is consistent with previous reports.[46–47] Thus, the 1T′-$MoTe_2$/WSe_2 Schottky photodetector is also designed to achieve the capability of polarization-sensing. **Figure 4a** shows the test scheme for polarization-resolved photodetection, the inset is an optical microscope image of the device. θ is the angle between the polarization direction of the incident light and the X-axis (armchair direction of the 1T′-$MoTe_2$ layer). The linearly polarized light can be converted from circularly polarized light by a polarizer, and illuminates on the device, then the polarized photocurrent at varied polarization angles (θ) can be achieved. It is noted that the light power at different polarization angles (0° to 360°) remains unchanged as shown in Figure S14 (Supporting Information), excluding the influence of light power on the change of photocurrent.

Figure 4b shows the polarization-dependent current mapping of the 1T′-$MoTe_2$/WSe_2 junction at different bias voltages under 635 nm polarized laser illumination, demonstrating that the photocurrent strongly relies on the polarization angle and bias voltage. To more visualize the polarization-sensitive photoresponse, the time-dependent photocurrent at zero bias by varying the polarization angles are measured in Figure 4c. It is observed that the photocurrent changes periodically when θ is rotated from 0° to 360°, and reaches maximum at θ of 0° (or 180°) corresponding to the armchair direction of 1T′-$MoTe_2$. The polarization ratio (PR), defined as photocurrent anisotropy ratio (I_{max}/I_{min}), can reach a maximum value of ≈30, which is exceeding the current level in most 2D-based polarized detectors.[1,2,4,9,11,12,14,16,28–45,48–53] The polarization-sensitive photodetection capability of the photovoltaic heterostructure device should be from the anisotropic 1T′-$MoTe_2$ component, as the individual WSe_2 has isotropic in-plane crystal structure and polarization-insensitive photoresponse, evidenced from that the Raman signal and photocurrent remain unchanged as function of the polarization angles of incident light as shown in Figures S15,S16 (Supporting Information).

The polarization-sensitive photodetection performances such as R, D^* and PR values are also compared among the detectors based on anisotropic 2D materials and heterojunctions (Table S1, Supporting Information). Most detectors have poor PR value less than 10 because of the low polarized light absorption, low carrier mobility and weak anisotropic properties. Notably, the new figures of merit including the polarization angle sensitivity (*PAS*) and polarization angle detectivity (*PAD*) have recently been proposed to evaluate the overall performance of a polarization-sensitive detector for more standard and fair assessment.[18] In our device, the *PAS* and *PAD* are calculated to be 0.022 A W^{-1} $degree^{-1}$ and 4.32×10^9 Jones/degree, respectively, which represent a high level particularly for the zero-biased photovoltaic detector as shown in Table S1 and Figure S17 (Supporting Information). Together with a high steady PR value of ≈30 and unique polarization- and gate-tunable optoelectronic reverse, our device can exhibit widespread application potential in future ultra-compact polarimeters. Furthermore, it is noticed that the

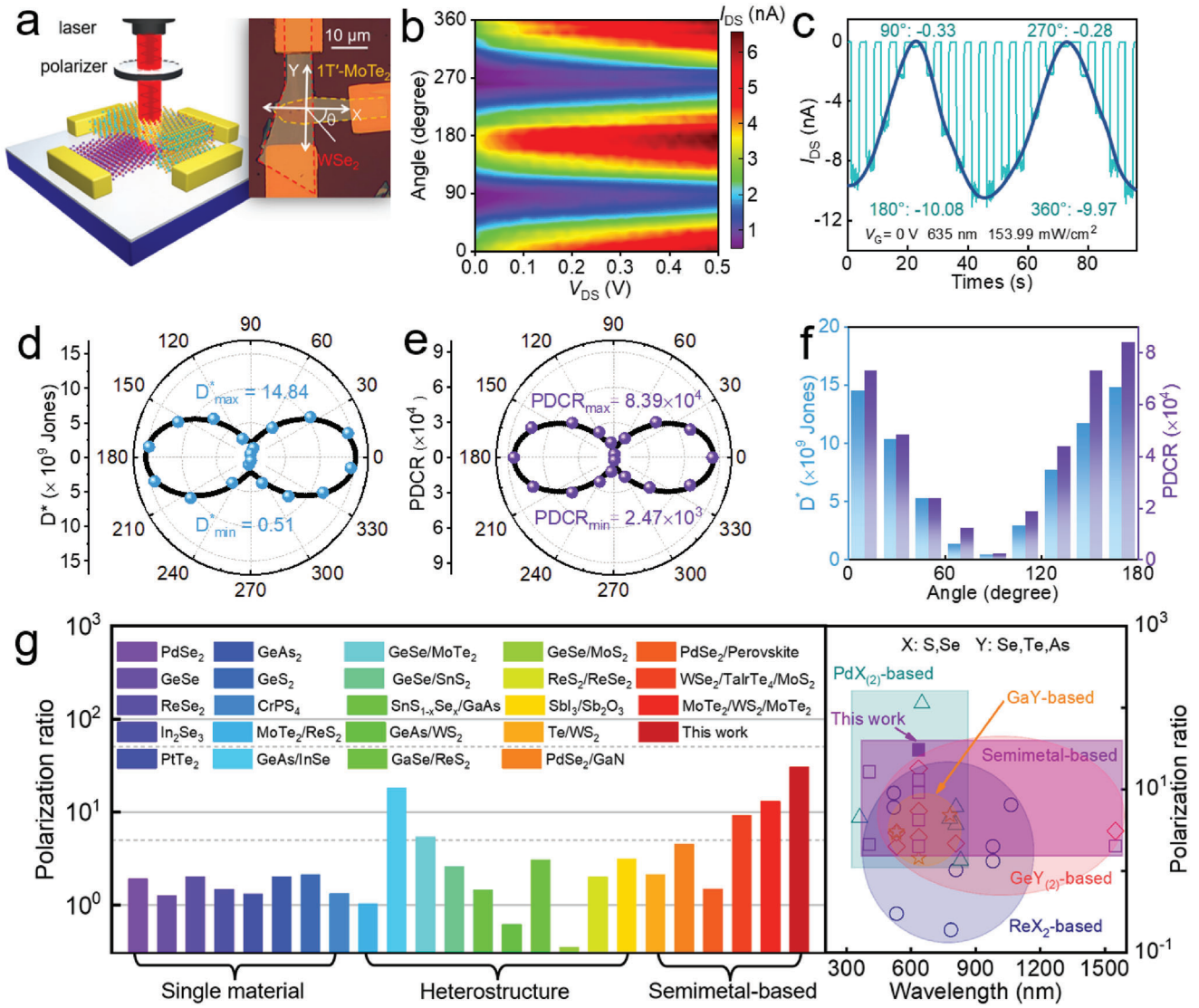

Figure 4. Polarimetric photodetection of the 1T′-$MoTe_2$/WSe_2 Schottky junction. a) Schematic diagram of the experimental setup for polarization-resolved photocurrent measurement. θ is the angle between the polarization direction of incident light and the *X* axis (armchair direction of the 1T′-$MoTe_2$). b) Polarization-dependent current mapping at various bias voltages under illumination at 635 nm (153.99 mW cm^{-2}). c) Time-resolved photocurrent under linearly polarized light with varying polarization angle from 0° to 360°. Polar diagram of the polarization-sensitive detectivity d) and photo–dark current ratio (*PDCR*) e) at light wavelength of 635 nm and at zero bias voltage. f) Histogram of detectivity and *PDCR* extracted from the polar diagram. g) Comparison of polarization ratio (PR) values among the reported 2D-based polarimetric photodetectors. The labels X represent S, Se, Y contains Se, Te, As. ($PdSe_2$,[11] GeSe,[14] $ReSe_2$,[9] In_2Se_3,[28] $PtTe_2$,[29] $GeAs_2$,[30] GeS_2,[31] $CrPS_4$,[32] $MoTe_2/ReS_2$,[33] GeAs/InSe,[34] $GeSe/MoTe_2$,[35] $GeSe/SnS_2$,[36] $SnS_{1-X}Se_x/GaAs$,[37] $GeAs/WS_2$,[38] $GaSe/ReS_2$,[48] $GeSe/MoS_2$,[39] $ReS_2/ReSe_2$,[40] SbI_3/Sb_2O_3,[41] Te/WS_2,[42] $PdSe_2/GaN$,[43] $PdSe_2$/Perovskite,[44] $WSe_2/TaIrTe_4/MoS_2$,[16] $MoTe_2/WS_2/MoTe_2$[45]).

PR value varies with different batches of devices, which may be caused by different thickness and contact or interface qualities in the devices. Figure S18 (Supporting Information) shows the statistical results, most devices have PR values in the range of 10–30, which can meet the market demands for polarization-resolved applications.

As a result of the polarimetric photocurrent, the device exhibits strong anisotropy in the key performance metrics such as *R*, *EQE*, D^*, and *PDCR*, from their polar plots (Figure 4d–f and Figure S19, Supporting Information), enabling the sensitive recognition of polarization information of incident light. Figure 4g shows the comparison of polarization ratio among the polarized photodetectors developed so far based on anisotropic 2D materials and heterostructures, our vdW Schottky photodetectors present much superior PR values, offering a promising platform for polarization-resolved imaging application.

2.5. Reverse in Photocurrent by Light Polarization

Following the gate-tunable reverse in rectifying and photovoltaic characteristics of the device as discussed above, the influence of

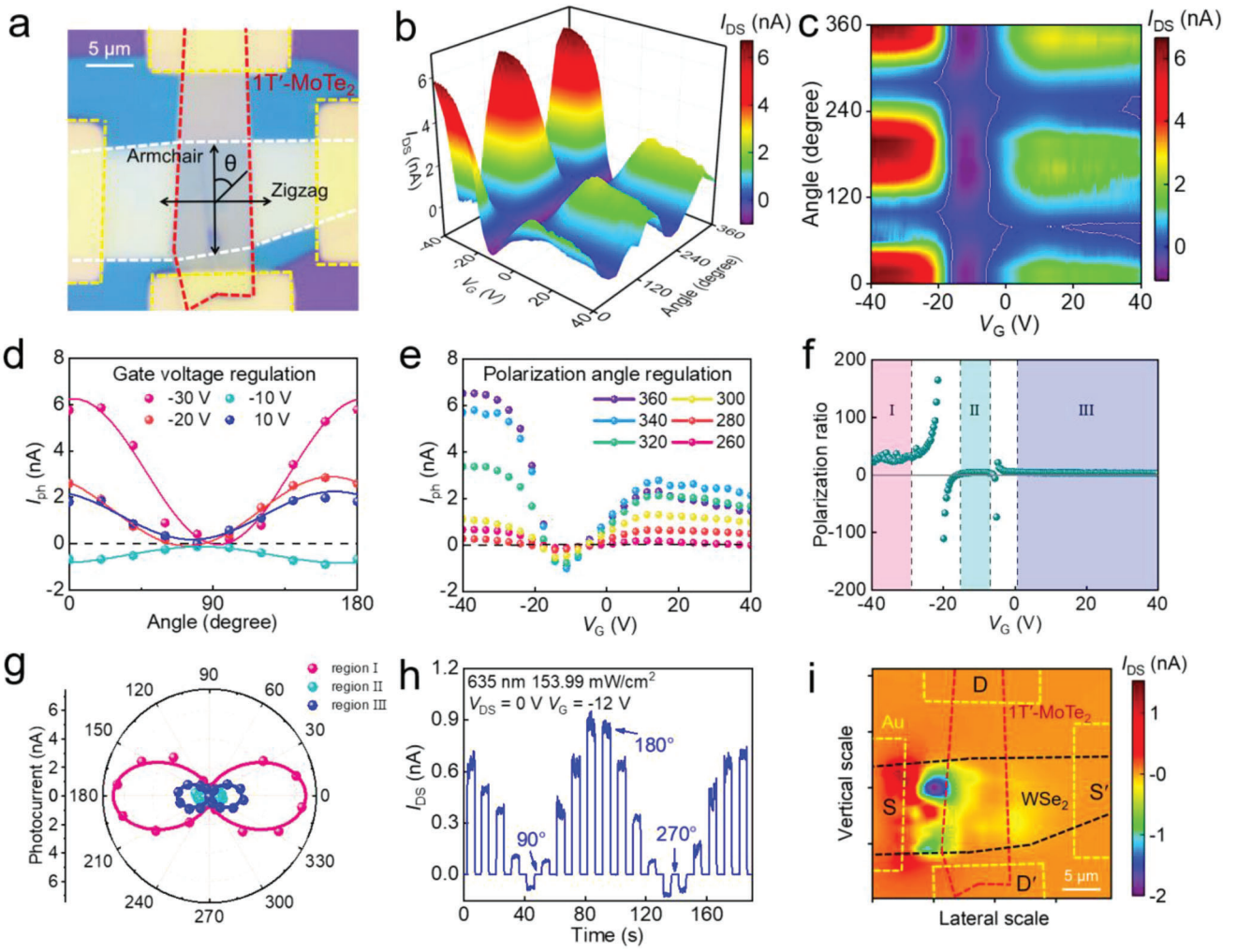

Figure 5. Gate-tunable and reversible polarization-sensitive photocurrent. a) Optical microscope images of the device. 3D color map b) and 2D contour plot c) of photocurrent distribution as a function of polarization angles and gate voltages at zero bias. d) Extracted I_{DS} as function of polarization angle at V_G of −30, −20, −10, and 10 V. e) Extracted I_{DS} as function of V_G under different light polarization. f) Calculated PR values as function of gate voltage. g) Polar diagram of the polarization-dependent photocurrent at different regions. h) Time-dependent photoresponse by varying polarization angles of incident 635 nm light at V_{DS} of 0 V and V_G of −12 V, showing a reverse in photocurrent induced by light polarization. i) Scanning photocurrent mapping of the device at zero bias, showing the opposite sign of photocurrent at Au/WSe_2 and 1T′-$MoTe_2$/WSe_2 interface. The light spot diameter is about 2 μm.

gate voltage on polarization-sensitive photoresponse is further investigated. As shown in the optical microscope image of the device (**Figure 5a**), θ is the angle between the polarization direction of incident light and the armchair direction of the 1T′-$MoTe_2$. The 3D and 2D contour plots of the polarized photocurrent distribution related to the gate voltage and polarization angles under 635 nm polarized light illumination are shown in Figure 5b,c. It is observed that the photocurrent changes periodically as function of polarization angles with a periodicity of 180°. The photocurrent by varying polarization angles and gate voltages are shown in Figure 5d,e, respectively, the device retains tunable polarization-sensitive capability, and the polarized photocurrent undergoes a sign transition between negative and positive by changing the polarization angles of incident light at specific range of gate voltage (−20 to 0 V).

The values of polarization ratio as function of V_G can be extracted from Figure 5c and plotted in Figure 5f. The PR values are strongly related with V_G, which can be divided into three steady-state regions: region I (−40 to −29 V), region II (−15 to -−7 V) and region III (0–40 V), respectively. Figure 5g (Figure S20, Supporting Information) shows the polar plots of polarized light excited photocurrent at the three regions, also clearly demonstrating the gate-tunable polarization sensitivity. Particularly, the calculated PR values show some divergent points with values reaching positive or negative infinity at both edges of region II. This abnormal phenomenon can step from the transition of photocurrent sign at V_G of −20–0 V. By varying polarization angles, the polarization-sensitive photocurrent increases (or decreases) gradually and approaches zero when the sign reversal occurs, leading to the divergent data toward infinity. Thus, the PR value (I_{max}/I_{min}) is mainly determined by the sign of I_{max} and I_{min}. It can keep steady when their signs are same (both are positive or negative). While, it changes rapidly when the sign of I_{min} is reversal. In such case, the distributions of PR values by varying the gate

voltages can be roughly classified into three steady-state regions and two rapidly changing regions. The phenomenon of infinite PR values is similar to the recently reported nanoantenna-mediated semimetal photodetectors where the PR values can cover a wide range (1→∞/-∞→−1) by tuning the antennas orientation.[24,54,55]

To further confirm the polarization-induced reverse in polarized photocurrent, the time-dependent dynamic photoresponse by varying the polarization angles at V_G of -12 V and V_{DS} of 0 V is shown in Figure 5h and Figure S21 (Supporting Information). It is clearly observed that the photocurrent varies with angles and has a sign reversal from positive to negative. It is hypothesized that this phenomenon may be related with the photocurrent generation at the two junctions of 1T′-$MoTe_2$/WSe_2 and Au/WSe_2 contact in our device. Figure 3g–i and Figure 5i illustrate the scanning photocurrent mapping of our device, the photocurrent with opposite direction can be distributed in WSe_2/Au region and WSe_2/1T′-$MoTe_2$ junction, the former is polarization-insensitive due to the isotropic crystal structure of WSe_2, the latter is polarization-sensitive because of the anisotropic crystal structure and anisotropic light absorption of 1T′-$MoTe_2$. The photocurrent from 1T′-$MoTe_2$/WSe_2 Schottky junction is defined as I_1, and the photocurrent caused by the Au/WSe_2 junction is defined as I_2. It is noted that I_1 is polarization-sensitive while I_2 is not. The total photocurrent value is $I_{total} = I_1 - I_2$, where the symbol "-" means the opposite direction of photocurrent. The equivalent-circuit diagram is plotted (Figure S22, Supporting Information) to show the components of photocurrent in the device at zero bias. During the measurement, the polarization-sensitive photocurrent (I_1) decreases and reaches minimum when the polarization angle of incident light is rotated along the zigzag direction of 1T′-$MoTe_2$. When the value of I_1 becomes smaller than that of I_2, the total photocurrent can be turned to be negative, leading to the sign reversal of photocurrent. This ability of polarization induced photocurrent flipping is of significant importance for our proof-of-concept polarimetric photodetector toward higher recognition rate and imaging resolution.

3. Conclusion

In summary, we have demonstrated the multifunctional photovoltaic heterostructure composed of semimetal 1T′-$MoTe_2$ with in-plane anisotropic structure and semiconducting WSe_2 with ambipolar transport. The photovoltaic detector exhibits a reverse phenomenon in both rectifying and photovoltaic characteristics, which can be attributed to the inversion of energy band bending and built-in field by the back-gate. The current rectification ratio is tuned in a broad range from 10^{-2} to 10^3. Acting as a polarimetric detector, the device achieves high performance metrics with ultra-low noise of ≈5 fA $Hz^{-1/2}$ and fast speed of ≈110 µs, enabling a clear imaging with 100 × 100 pixels. The PR can reach a steady value exceeding ≈30, which is compelling among the state-of-the-art 2D-based polarized detectors and can meet the market demands for polarimetric imaging. As a more promising capability, the device exhibits a sign reversal of polarization-sensitive photocurrent by varying the light polarization angles, resulting in a possibility of PR value reaching infinity, that may provide a unique perspective for polarization signal recognition and imaging. This work makes a conceptual advance in designing different device scheme and mechanism to achieve optoelectronic reverse phenomenon and high polarization-sensitive detection performance, which can pave the way for an integration of the multiple functional modules into a single module toward "All-in-one" system.

4. Experimental Section

Device Fabrication: Multilayer 1T′-$MoTe_2$ and WSe_2 nanosheets were micromechanically exfoliated from the bulk crystal (Shanghai OnWay Technology Co., Ltd) using the scotch-tape on the SiO_2 (300 nm)/Si substrate. The 1T′-$MoTe_2$/WSe_2 Schottky junctions were fabricated by the dry-transfer method. In this process, the 1T′-$MoTe_2$ layer was stacked with WSe_2 layer by using the PVA/PDMS assisted dry-transfer method. In short, The PVA solution was injected on top of the PDMS film placed in the center of the slide and then the solid PVA/PDMS film can be obtained by heating at 60 °C for 5 min. Subsequently, contact the target 1T′-$MoTe_2$ nanosheet on the SiO_2/Si substrate with the PVA side of the solid film, heating at 90 °C for 3–5 min. Afterward, the solid film with 1T′-$MoTe_2$ was separated from the silicon substrate and continues to contact the target WSe_2 on the substrate to form Schottky junction. The substrate with the junction was treated with ozone and then the photoresist (An ARP-5350 positive photoresist bought from Taizhou SUNANO New Energy Co., Ltd.) was spin-coated onto the substrate at 3000 rpm for 60 s. After being baked on a hot plate for 4 min at 100°C, the substrate was exposed to ultraviolet laser with a lithography machine (TuoTuo Technology (Suzhou) Co., Ltd.). The chip was developed by using a developing solution, cleaned by deionized water and dried by N_2 gas. Finally, the electron-beam evaporation instrument was employed to define and deposit contact electrodes (50 nm Au).

First-Principles Calculation: The first-principles calculations were carried out using Vienna ab Initio Simulation Package (VASP)[56,57] based on the frozen-core projector augmented wave (PAW) method within the framework of the density functional theory (DFT). The electron exchange-correlation interaction was characterized by the generalized gradient approximation (GGA) in the form of the Perdew–Burke–Ernzerhof (PBE) functional including van der Waals correlations proposed by Grimme.[58] A cut-off energy of 400 eV was adopted for the Kohn–Sham orbitals expansion in a plane-wave basis. The energy and force convergence criteria were set to less than 10^{-3} meV and 0.01 eV $Å^{-1}$, respectively. *k*-point meshes were set to 9 × 16 × 1 and 16 × 16 × 1 for 1T′-$MoTe_2$ and WSe_2 nanosheets, respectively.

Characterization: Raman spectra were measured by a Raman instrument (Nost Technology Co., Ltd, a laser excitation of 532 nm and spot size of 10 µm) in ambient conditions. The thickness of the sample and the contact potential difference of the interface could be tested using a Scanning Probe Microscope (SPM) with the functional modules of AFM and KPFM (Oxford Cypher S AFM. Co., Ltd.). The electrical transport of the device was measured via a four-probe station (PSAICPB6A, PRECISION SYSTEMS INDUSTRIAL Co., Ltd.) equipped with a KEITHLEY 2636B semiconductor source meter. The photoresponse was tested using a 405 and 635 nm optical fiber laser. The spot diameter of all the excitation lasers was ≈3 mm and the response time was extracted via a shutter system with a modulator–demodulator function. The imaging system was equipped with a camera lens (CAV-SPRATDS-V2), a 2D rotary stage (MDOM103) and an amplification circuit. The dark current traces of the device were measured with the KEITHLEY 2636B semiconductor source meter at $V_{DS} = V_G = 0$ V with a sampling rate of 50 Hz. The noise spectral density (S_n) was then obtained by calculating the Fourier transformation of dark current traces. Single-pixel imaging and scanning photocurrent mapping measurements were conducted by a photocurrent imaging instrument (Mstarter 200 High Precision Photocurrent Scanning Test Microscope) (supplied by Nanjing Metatest Optoelectronic Technology Co., Ltd.).

Supporting Information

Supporting Information is available from the Wiley Online Library or from the author.

Acknowledgements

The authors acknowledge financial support from the National Natural Science Foundation of China (Nos. 11904108, 62004071, 62125404), the China Postdoctoral Science Foundation (No.2020M672680), the "The Pearl River Talent Recruitment Program" (No.2019ZT08×639), Beijing Natural Science Foundation (Z220005), the Strategic Priority Research Program of Chinese Academy of Sciences (Grant No. XDB43000000), and the CAS-JSPS Cooperative Research Project (No. GJHZ2021131).

Conflict of Interest

The authors declare no conflict of interest.

Data Availability Statement

Research data are not shared.

Keywords

gate voltage, light polarization, optoelectronic reverse, Polarimetric photodetector, Schottky junction

Received: September 11, 2023
Revised: September 27, 2023
Published online: December 5, 2023

[1] H.-Y. Hou, S. Tian, H.-R. Ge, J.-D. Chen, Y.-Q. Li, J.-X. Tang, *Adv. Funct. Mater.* **2022**, *32*, 2209324.
[2] D. Wu, J. Guo, J. Du, C. Xia, L. Zeng, Y. Tian, Z. Shi, Y. Tian, X. J. Li, Y. H. Tsang, J. Jie, *ACS Nano* **2019**, *13*, 9907.
[3] J. Wang, C. Jiang, W. Li, X. Xiao, *Adv. Opt. Mater.* **2022**, *10*, 2102436.
[4] Z. Guo, R. Cao, H. Wang, X. Zhang, F. Meng, X. Chen, S. Gao, D. K. Sang, T. H. Nguyen, A. T. Duong, J. Zhao, Y.-J. Zeng, S. Cho, B. Zhao, P.-H. Tan, H. Zhang, D. Fan, *Natl. Sci. Rev* **2021**, *9*, nwab098.
[5] J. Yu, X. Kuang, Y. Gao, Y. Wang, K. Chen, Z. Ding, J. Liu, C. Cong, J. He, Z. Liu, Y. Liu, *Nano Lett.* **2020**, *20*, 1172.
[6] S. Han, W. Jin, D. Zhang, T. Tang, C. Li, X. Liu, Z. Liu, B. Lei, C. Zhou, *Chem. Phys. Lett.* **2004**, *389*, 176.
[7] Z. Fan, P.-C. Chang, J. G. Lu, E. C. Walter, R. M. Penner, C.-H. Lin, H. P. Lee, *Appl. Phys. Lett.* **2004**, *85*, 6128.
[8] C. Wu, J. Jie, L. Wang, Y. Yu, Q. Peng, X. Zhang, J. Cai, H. Guo, D. Wu, Y. Jiang, *Nanotechnology* **2010**, *21*, 505203.
[9] E. Zhang, P. Wang, Z. Li, H. Wang, C. Song, C. Huang, Z.-G. Chen, L. Yang, K. Zhang, S. Lu, W. Wang, S. Liu, H. Fang, X. Zhou, H. Yan, J. Zou, X. Wan, P. Zhou, W. Hu, F. Xiu, *ACS Nano* **2016**, *10*, 8067.
[10] Z. Zhou, M. Long, L. Pan, X. Wang, M. Zhong, M. Blei, J. Wang, J. Fang, S. Tongay, W. Hu, J. Li, Z. Wei, *ACS Nano* **2018**, *12*, 12416.
[11] J. Zhong, J. Yu, L. Cao, C. Zeng, J. Ding, C. Cong, Z. Liu, Y. Liu, *Nano Res.* **2020**, *13*, 1780.
[12] H. Yuan, X. Liu, F. Afshinmanesh, W. Li, G. Xu, J. Sun, B. Lian, A. G. Curto, G. Ye, Y. Hikita, Z. Shen, S.-C. Zhang, X. Chen, M. Brongersma, H. Y. Hwang, Y. Cui, *Nat Nanotechnol* **2015**, *10*, 707.
[13] F. Liu, S. Zheng, X. He, A. Chaturvedi, J. He, W. L. Chow, T. R. Mion, X. Wang, J. Zhou, Q. Fu, H. J. Fan, B. K. Tay, L. Song, R.-H. He, C. Kloc, P. M. Ajayan, Z. Liu, *Adv. Funct. Mater.* **2016**, *26*, 1169.
[14] X. Wang, Y. Li, L. Huang, X.-W. Jiang, L. Jiang, H. Dong, Z. Wei, J. Li, W. Hu, *J. Am. Chem. Soc.* **2017**, *139*, 14976.
[15] J. Wang, H. Wang, Q. Chen, L. Qi, Z. Zheng, N. Huo, W. Gao, X. Wang, J. Li, *Appl. Phys. Lett.* **2022**, *121*, 103502.
[16] X. Han, P. Wen, L. Zhang, W. Gao, H. Chen, F. Gao, S. Zhang, N. Huo, B. Zou, J. Li, *ACS Appl. Mater. Interfaces* **2021**, *13*, 61544.
[17] X. Wang, J. Shang, M. Zhu, X. Zhou, R. Hao, L. Sun, H. Xu, J. Zheng, X. Lei, C. Li, L. Kou, Q. Feng, *Nanoscale Horiz.* **2020**, *5*, 954.
[18] M. Dai, C. Wang, B. Qiang, Y. Jin, M. Ye, F. Wang, F. Sun, X. Zhang, Y. Luo, Q. J. Wang, *Nat. Commun.* **2023**, *14*, 3421.
[19] M. Dai, C. Wang, B. Qiang, F. Wang, M. Ye, S. Han, Y. Luo, Q. J. Wang, *Nat. Commun.* **2022**, *13*, 4560.
[20] M. Dai, C. Wang, M. Ye, S. Zhu, S. Han, F. Sun, W. Chen, Y. Jin, Y. Chua, Q. J. Wang, *ACS Nano* **2022**, *16*, 295.
[21] W. Deng, M. Dai, C. Wang, C. You, W. Chen, S. Han, J. Han, F. Wang, M. Ye, S. Zhu, J. Cui, Q. J. Wang, Y. Zhang, *Adv. Mater.* **2022**, *34*, 2203766.
[22] J. Wei, Y. Li, L. Wang, W. Liao, B. Dong, C. Xu, C. Zhu, K.-W. Ang, C.-W. Qiu, C. Lee, *Nat. Commun.* **2020**, *11*, 6404.
[23] D. J. Kim, M. Alexe, *Appl. Phys. Lett.* **2017**, *110*, 183902.
[24] J. Wei, C. Xu, B. Dong, C.-W. Qiu, C. Lee, *Nat. Photonics* **2021**, *15*, 614.
[25] X. Lu, L. Sun, P. Jiang, X. Bao, *Adv. Mater.* **2019**, *31*, 1902044.
[26] Q. Qiu, Z. Huang, *Adv. Mater.* **2021**, *33*, 2008126.
[27] Y. Chen, X. Wang, G. Wu, Z. Wang, H. Fang, T. Lin, S. Sun, H. Shen, W. Hu, J. Wang, J. Sun, X. Meng, J. Chu, *Small* **2018**, *14*, 1703293.
[28] S. Wang, Z. Yang, D. Wang, C. Tan, L. Yang, Z. Wang, *ACS Appl. Mater. Interfaces* **2023**, *15*, 3357.
[29] T. Wei, X. Wang, Q. Yang, Z. He, P. Yu, Z. Xie, H. Chen, S. Li, S. Wu, *ACS Appl. Mater. Interfaces* **2021**, *13*, 22757.
[30] L. Li, P. Gong, D. Sheng, S. Wang, W. Wang, X. Zhu, X. Shi, F. Wang, W. Han, S. Yang, K. Liu, H. Li, T. Zhai, *Adv. Mater.* **2018**, *30*, 1804541.
[31] Y. Yang, S.-C. Liu, X. Wang, Z. Li, Y. Zhang, G. Zhang, D.-J. Xue, J.-S. Hu, *Adv. Funct. Mater.* **2019**, *29*, 1900411.
[32] H. Zhang, Y. Li, X. Hu, J. Xu, L. Chen, G. Li, S. Yin, J. Chen, C. Tan, X. Kan, L. Li, *Appl. Phys. Lett.* **2021**, *119*, 171102.
[33] J. Ahn, J.-H. Kyhm, H. K. Kang, N. Kwon, H.-K. Kim, S. Park, D. K. Hwang, *ACS Photonics* **2021**, *8*, 2650.
[34] J. Xiong, Y. Sun, L. Wu, W. Wang, W. Gao, N. Huo, J. Li, *Adv. Opt. Mater.* **2021**, *9*, 2101017.
[35] N. Zhang, L. Wu, W. Gao, Q. Zhao, N. Huo, J. Li, *Adv. Mater. Interfaces* **2022**, *9*, 2200150.
[36] L. Wu, W. Gao, Y. Sun, M. Yang, Z. Zheng, W. Fan, K. Shu, Z. Dan, N. Zhang, N. Huo, J. Li, *Adv. Mater. Interfaces* **2022**, *9*, 2102099.
[37] M. Yang, W. Gao, M. He, S. Zhang, Y. Huang, Z. Zheng, D. Luo, F. Wu, C. Xia, J. Li, *Nanoscale* **2021**, *13*, 15193.
[38] J. Xiong, Z. Dan, H. Li, S. Li, Y. Sun, W. Gao, N. Huo, J. Li, *ACS Appl. Mater. Interfaces* **2022**, *14*, 22607.
[39] Y. Xin, X. Wang, Z. Chen, D. Weller, Y. Wang, L. Shi, X. Ma, C. Ding, W. Li, S. Guo, R. Liu, *ACS Appl. Mater. Interfaces* **2020**, *12*, 15406.
[40] K. Li, C. Du, H. Gao, T. Yin, L. Zheng, J. Leng, W. Wang, *ACS Appl. Mater. Interfaces* **2022**, *14*, 33589.
[41] M. Xiao, H. Yang, W. Shen, C. Hu, K. Zhao, Q. Gao, L. Pan, L. Liu, C. Wang, G. Shen, H.-X. Deng, H. Wen, Z. Wei, *Small* **2020**, *16*, e1907172.
[42] Z. Luo, H. Xu, W. Gao, M. Yang, Y. He, Z. Huang, J. Yao, M. Zhang, H. Dong, Y. Zhao, Z. Zheng, J. Li, *Small* **2023**, *19*, 2207615.
[43] D. Wu, M. Xu, L. Zeng, Z. Shi, Y. Tian, X. J. Li, C.-X. Shan, J. Jie, *ACS Nano* **2022**, *16*, 5545.
[44] L.-H. Zeng, Q.-M. Chen, Z.-X. Zhang, D. Wu, H. Yuan, Y.-Y. Li, W. Qarony, S. P. Lau, L.-B. Luo, Y. H. Tsang, *Adv. Sci.* **2019**, *6*, 1901134.
[45] J. Wu, D. Luo, P. Wen, X. Han, C. Wang, H. Yu, W. Gao, X. Liu, G. Konstantatos, J. Li, N. Huo, *Adv. Opt. Mater.* **2022**, *10*, 2201902.
[46] G. H. Han, D. H. Keum, J. Zhao, B. G. Shin, S. Song, J. J. Bae, J. Lee, J. H. Kim, H. Kim, B. H. Moon, Y. H. Lee, *2D Mater.* **2016**, *3*, 031010.
[47] R. Beams, L. G. Cançado, S. Krylyuk, I. Kalish, B. Kalanyan, A. K. Singh, K. Choudhary, A. Bruma, P. M. Vora, F. Tavazza, A. V. Davydov, S. J. Stranick, *ACS Nano* **2016**, *10*, 9626.

[48] S. Quan, S. Guo, D. Weller, S. Fu, Y. Wang, R. Liu, *ACS Appl. Nano Mater.* **2022**, *5*, 7365.
[49] Q. Zhao, F. Gao, H. Chen, W. Gao, M. Xia, Y. Pan, H. Shi, S. Su, X. Fang, J. Li, *Mater. Horiz.* **2021**, *8*, 3113.
[50] Y. Cui, Z. Zhou, X. Wang, X. Wang, Z. Ren, L. Pan, J. Yang, *Nano Res.* **2021**, *14*, 2224.
[51] S. Mukherjee, K. Das, S. Das, S. K. Ray, *ACS Photonics* **2018**, *5*, 4170.
[52] Y. Yu, T. Xiong, Z. Guo, S. Hou, J. Yang, Y.-Y. Liu, H. Gu, Z. Wei, *Fundam. Res.* **2022**, *2*, 985.
[53] Z. Zhou, M. Long, L. Pan, X. Wang, M. Zhong, M. Blei, J. Wang, J. Fang, S. Tongay, W. Hu, J. Li, Z. Wei, *ACS Nano* **2018**, *12*, 12416.
[54] J. Wei, Y. Chen, Y. Li, W. Li, J. Xie, C. Lee, K. S. Novoselov, C.-W. Qiu, *Nat. Photonics* **2022**, *17*, 171.
[55] J. Xie, Z. Ren, J. Wei, W. Liu, J. Zhou, C. Lee, *Adv. Opt. Mater.* **2023**, *11*, 2202867.
[56] G. Kresse, J. Hafner, *J. Phys.: Condens. Matter* **1994**, *6*, 8245.
[57] G. Kresse, J. Furthmüller, *Phys. Rev. B: Condens. Matter Mater. Phys.* **1996**, *54*, 11169.
[58] S. Grimme, *J. Comput. Chem.* **2006**, *27*, 1787.